

Article

Not peer-reviewed version

---

# A Multi-Modality Fusion and Gated Multi-Filter U-net for Water Area Segmentation of Remote Sensing

---

[Rong.fang.Wang](#)<sup>\*</sup>, Chen.chen.Zhang, [Chao.Chen](#), [Hong.xia.Hao](#), [Wei.bin.Li](#), [Li.cheng.Jiao](#)

Posted Date: 15 December 2023

doi: 10.20944/preprints202312.1143.v1

Keywords: water area segmentation; multi-modality fusion; multi-filter inception; attention mechanism; remote sensing




Preprints.org is a free multidiscipline platform providing preprint service that is dedicated to making early versions of research outputs permanently available and citable. Preprints posted at Preprints.org appear in Web of Science, Crossref, Google Scholar, Scilit, Europe PMC.

Copyright: This is an open access article distributed under the Creative Commons Attribution License which permits unrestricted use, distribution, and reproduction in any medium, provided the original work is properly cited.

## Article

# A Multi-modality Fusion and Gated Multi-filter U-Net for Water Area Segmentation of Remote Sensing

Rongfang Wang <sup>1,\*</sup> , Chenchen Zhang <sup>1</sup>, Chao Chen <sup>2</sup>, Hongxia Hao <sup>3</sup>, Weibin Li <sup>1</sup> and Licheng Jiao <sup>1</sup>

<sup>1</sup> School of Artificial Intelligence, Xidian University, Xi'an, China

<sup>2</sup> IBM Research, Silicon Valley Lab, San Jose, CA, United States

<sup>3</sup> School Of Computer Science and Technology, Xidian University, Xi'an, China

\* Correspondence: rfwang@xidian.edu.cn

**Abstract:** Water area segmentation in remote sensing is of great importance for flood monitoring. To overcome some challenges in this task, we construct the Water Index and Polarization Information (WIPI) multi-modality dataset and propose a multi-Modality Fusion and Gated multi-Filter U-Net (MFGF-UNet) convolutional neural network. The WIPI dataset could enhance the water information while reducing the data dimension, especially, the Cloud-Free Label provided in the dataset could effectively alleviate the problem of labeled sample scarcity. Since a single form or uniform kernel size cannot handle the variety in size and shape of water bodies, we proposed the gated multi-filter inception (GMF-Inception) module in our MFGF-UNet. Moreover, we utilize the attention mechanism by introducing the Gated Channel Transform (GCT) skip connection and integrating GCT into GMF-Inception to further improve model performance. Extensive experiments on three benchmarks, including WIPI, Chengdu and GF2020 datasets demonstrate that our method achieves favorable performance with lower complexity and better robustness against six competing approaches. For example, on WIPI, Chengdu and GF2020 datasets, the proposed MFGF-UNet model achieves F1 of 0.9191, 0.7410, and 0.8421, respectively, which average F1 on three datasets is 0.0045 higher than the U-Net model and reduces 62% average GFLOPs. New WIPI dataset, code and trained models have been released on GitHub.

**Keywords:** water area segmentation; multi-modality fusion; multi-filter inception; attention mechanism; remote sensing

## 1. Introduction

Detection of surface water area is essential for water resource management, flood identification, and ecological protection[1]. Satellite remote sensing images have the advantages of large coverage, low cost, and short data acquisition period, and are often used in water area analysis.[2–4]. The key to accurately segmenting water areas from complex ground features and creating water area maps lies in effectively highlighting water bodies.

Spectral data is the first choice for creating water area maps in cloudless conditions. It can provide multi-band remote sensing images with high resolution and less noise. The disadvantage of spectral image is that spectral imager is a passive imaging instrument, which needs sunlight to provide a light source, so it cannot provide satellite image all day long, and the acquired image will have information loss due to the light being blocked by clouds. Synthetic Aperture Radar (SAR), which is based on imaging of backscattered polarization information, can detect water areas without cloud interference and take images of the ground all day long. However, polarization information of SAR images cannot distinguish water, water-like surfaces and noise-like spots well[5]. These defects may limit the application of polarization information in water segmentation. Therefore, the combination of spectral data and SAR helps to improve the effect of automatic water segmentation.

In early studies, water areas segmentation was limited by remote sensing technology and image quality[6]. In low-resolution remote sensing images, threshold filtering can only be carried out by the different radiation intensities of water in different bands. However, when threshold filtering is applied directly to the original imaging data, an accurate segmentation map cannot be obtained in most cases. Therefore, a water index method has been developed. The water index-based methods make use of the intrinsic nature that water bodies have different reflectance under different wavelengths. Thereby, we can choose multiple bands from spectral imaging data and combine them to highlight water bodies and inhibit other ground objects[7]. And then, a threshold method is used to filter the calculated water index to extract the water areas. However, for the threshold method, it is difficult to determine an appropriate threshold value that can adapt to any complex ground environment. Under different water indexes from different scenarios, the threshold value is not uniform. In order to solve the above issues, some researchers start to establish a water segmentation algorithm based on machine learning for reducing the dependence on threshold, such as Random Forest (RF)[8], Support Vector Machine (SVM)[9], Decision Tree (DT) and Deep Neural Networks (DNN) [10,11].

Compared with other machine learning methods, DNN based on deep learning has a strong ability for automatic feature extraction and is able to learn semantic, high-level, and deeper features. Therefore, more powerful automatic segmentation methods of deep learning-based are proposed, especially Convolutional Neural Network (CNN)-based. Long *et al.*[12] have proposed a Fully Convolutional Network (FCN), which is used for natural image semantic segmentation for the first time. FCN replaces the fully connected layers of a pre-trained convolutional neural network, such as VGG16[13], with fully convolutional layers. It allows the network to accept input images of arbitrary size and uses upsampling to restore the size of output, thus achieving end-to-end mapping from the input image to the output segmentation map. A U-shaped convolutional network (U-Net) is an improvement on the FCN architecture by Ronneberger *et al.*[14] in 2015 and is applied to medical image segmentation. The U-Net consists of an encoder (down-sampling path) and a decoder (up-sampling path) connected by skip connections. Due to its simple structure, U-Net can achieve high accuracy with limited training samples which makes it and its series of extensions have been widely used in various image segmentation tasks, including remote sensing image segmentation[15,16]. Deeplabs[17–19] are another series of CNN-based models for image semantic segmentation that have been proposed and iteratively improved by the Google team. Among them, Deeplabv3+[19] is the latest version, in which the model performs convolution operations by employing parallel atrous convolutions at various rates to capture contextual features at multiple scales. Boundary-Aware Salient Object Detection Network (BASNet)[20] is proposed by Qin *et al.* in 2019 for salient detection and water segmentation tasks. BASNet generates coarse prediction maps using the encoder-decoder network, and then refines the coarse prediction maps with the ResNet34[21] refinement module to improve the performance. For solving some difficulties existing in water areas segmentation, such as complex background, huge scale, water connectivity, and rough edges, Liu *et al.* have proposed Dense U-Net Plus Network (DUPNet) in 2022 which is also based on U-Net architecture. DUPNet integrates Dense Block modules from DenseNet[22] and Multi-Scale Spatial Pyramid Pooling (MSPP) modules from DeeplabV3+. Dense Block is employed as the feature extraction module for both encoder and decoder, while MSPP is utilized for skip connections. In recent years, models based on self-attention mechanisms have made significant progress in computer vision tasks, particularly with the emergence of Vision Transformer (ViT)[23]. However, ViT-based architectures are generally parameter-heavy and require more labeled samples and computing resources. SegNeXt[24] is a popular convolutional attention network for semantic segmentation proposed by Guo *et al.* in 2022. SegNeXt delicately designs a convolutional attention that encodes contextual information more efficiently than self-attention in Transformers.

Among the above different methods, improved methods based on the U-Net have received more attention from researchers for water segmentation tasks. In the U-Net framework, the encoder module obtains high-level semantic information by extracting features from images layer by layer, while the decoder module collects different levels of semantic information and gradually recovers

spatial information of features. Based on this simple and effective encoder-decoder network, Goutam Konapala et al.[2] successfully drew a flood inundation map. They used the inundation data of 11 global flood events as samples to conduct training on the U-shaped convolutional network. Peri Akiva et al.[25] proposed a self-supervised flood segmentation model via adversarial domain adaptation and label refinement. In this model, a refiner is added to refine the rough mask obtained by the threshold method on the improved normalized differential water index, and finally improve the accuracy of flood segmentation.

Although the emergence of deep learning technology has greatly improved the accuracy and efficiency of water area segmentation, but there are still following challenges: 1) Remote sensing images usually include a wide range of ground, so the region of non-water contains complex and diverse ground object information and occupies a relatively large proportion, while the water area is generally small. It is a typical class imbalance problem. 2) Usually, there are water bodies of different sizes and shapes in remote sensing images, including from thousands of pixels to just a few pixels. In this case, using a single form or uniform kernel size in convolution operation cannot obtain good segmentation results. 3) Compared with natural images, remote sensing images have more interference and noise, which will affect the accuracy of water segmentation. Meanwhile, in the case of high-altitude shooting, the water area under the cloud shadow cannot be effectively separated by multispectral image, so it is necessary to utilize multi-modality data to obtain complementary information. 4) In existing multi-modality methods for water segmentation, direct superposition of original data or features is generally adopted for the use of multi-modality data. This simple superposition method cannot effectively extract the complementary features between different modalities but will produce many redundant features, affecting the final segmentation results.

To overcome the aforementioned challenges, we construct the Water Index and Polarization Information (WIPI) multi-modality dataset and propose a multi-Modality Fusion and Gated multi-Filter U-Net (MFGF-UNet) convolutional neural network for water area segmentation of remote sensing. Water indexes are initially used in threshold-based unsupervised methods for water body extraction. The water index is calculated by combining imaging information from different bands utilizing the strong absorption and low radiation of water in the wavelength range from visible light to infrared. After calculation, the pixel value of the combined band shows a relatively obvious difference between water and non-water materials, which can be used to segment water bodies by setting an appropriate threshold. After years of development, various water indexes have been proposed. McFeeters et. al.[26] proposed a Normalized Difference Water Index (NDWI) and used it in water body segmentation of multispectral images. Xu et al.[27] proposed a modified NDWI (MNDWI) by replacing the near-infrared band with the short-wave infrared band. Previous studies have shown that MNDWI is more suitable for enhancing water information and can extract water bodies more accurately than NDWI. In addition to the above two water indices, many researchers have proposed water indexes for other scenarios. In this work, to enhance water information while reducing the channel dimension of data, we analyze the characteristics of the water index and extract seven water indexes from 13 bands of raw multispectral images. However, multispectral images have large areas covered by clouds, which are defined as invalid areas and cannot participate in training. Therefore, based on the extracted water index, we fuse SAR polarization information for constructing WIPI multi-modality dataset. Moreover, we propose a Multi-Model Decision Fusion (MMDF) method to automatically obtain cloud-free labels to alleviate the problem of labeled sample scarcity and class imbalance in water segmentation.

Meanwhile, another promising advancement in the computer vision field is attention mechanisms, in which networks can allocate more resources to important regions in an image. Currently, attention mechanisms have been widely applied in many visual tasks, such as image classification[28,29], object detection[30,31], semantic segmentation[32,33], medical image processing[34,35], 3D vision[36], and multimodal tasks[37,38]. Gated Channel Transformation (GCT)[21] is a type of channel attention mechanism, which explicitly models the relationships between channels in feature maps using learnable variables. These learnable variables can determine the competitive or cooperative behavior

of neurons. Compared to Squeeze-and-Excitation (SE) Networks[28], GCT greatly reduces the number of parameters and computational complexity by introducing channel normalization layers. Thereby, in our MFGF-UNet model, we replace the direct skip connection of UNet with the GCT skip connection for adaptively focusing on more meaningful channel information and enhancing inter-channel feature extraction. Furthermore, since water bodies vary significantly in size and shape, to avoid the limitations brought by the single convolution form and uniform kernel size, as well as fully utilizing the multi-modality information of the constructed WIPI dataset, we design the gated multi-filter inception module between the input and U-shape backbone.

Finally, our MFGF-UNet model is compared to six other methods on three water segmentation datasets, including our constructed WIPI dataset, Chengdu dataset and GF2020 dataset. These datasets contain multispectral, SAR, and optical multi-modality images, cover different regions and are captured at different times. Extensive experiments of performance and complexity analysis show that our MFGF-UNet outperforms various competing methods.

To sum up, the main contributions of this paper are as follows:

- Releasing the Water Index and Polarization Information multi-modality dataset for water area segmentation of remote sensing. The proposed datasets are the first-ever to provide both water index modal and corresponding polarization information modal. Especially, the dataset contains the Cloud-Free Label automatically obtained by the proposed Multi-Model Decision Fusion algorithm, it could effectively alleviate the problem of labeled sample scarcity.
- We propose a multi-modality fusion and gated multi-filter U-shaped convolutional neural network, which introduces the GCT skip connection for adaptively focusing on more meaningful channels, as well as incorporates the proposed gated multi-filter inception module for fully utilizing the multi-modality information and handling the challenge due to the variety of water bodies in size and shape.
- Extensive experiments on three benchmarks, including WIPI (water index and SAR images), Chengdu (multispectral images) and GF2020 (optical images) datasets demonstrated that our MFGF-UNet model achieves favorable performance with lower complexity and better robustness against six competing approaches.

## 2. WIPI multi-modality dataset construction

### 2.1. Original Sen1Floods11 Dataset

The original data used to construct the Water Index and Polarization Information (WIPI) multi-modality dataset is derived from the Sen1Floods11<sup>1</sup>[39] dataset, which consists of the raw Sentinel-1 SAR image (Sen1-SAR) and the raw Sentinel-2 multispectral image (Sen2-MS), where Sen1-SAR includes VV and VH two bands, and Sen2-MS includes 13 bands (1-8, 8A, 9-12) across all spectrums. The format and bands description of the Sen1Floods11 is shown in Appendix Table A1. The Sen1Floods11 dataset is a surface water dataset covering 120,406 km<sup>2</sup>, and six continents of the world across 11 flood events. The event is selected by the requirements that the flood event had coverage from Sentinel-1, as well as coincident Sentinel-2 image on the same day or within 2 days of the Sentinel-1 image. Except for images, Sen1-SAR provides automated labels by the Otsu threshold method(Otsu Label-SAR), including two classes: water (label '1') and non-water (label '0'), and Sen2-MS provides manual labels(Manual Label-MS), including three classes: water (label '1'), non-water (label '0'), and cloud and invalid region (label '-1'). A set of sample images and masks from the Sen1Floods11 dataset are shown in Figure 1.

<sup>1</sup> <https://github.com/cloudtostreet/Sen1Floods11>



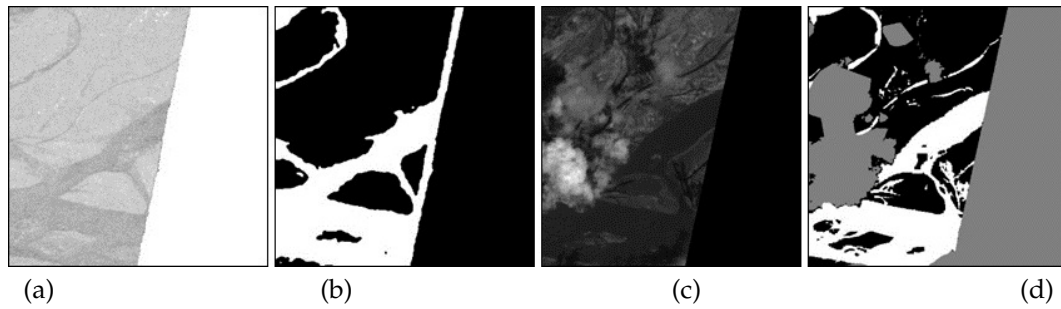


**Figure 1.** A set of sample images and masks from the Sen1Floods11 dataset. (a) Sen1-SAR Image (Band VV), (b) Otsu Label-SAR, (c) Sen2-MS Image (Band 8), (d) Manual Label-MS

## 2.2. Water Index Extraction

In this work, instead of directly superimposing the SAR and multispectral image, we first analyze the characteristics of the water index and extract seven water indexes from 13 bands of raw MSI to enhance water information while reducing the channel dimension of data. The seven extracted water indexes are: 1) Normalized Difference Vegetation Index (NDVI)[40]; 2) Normalized Difference Moisture Index (NDMI)[41]; 3) Normalized Difference Water Index (NDWI)[26]; 4) Modified Normalized Difference Water Index (MNDWI)[27]; 5) Automated Water Extraction Index Non-Shadow (AWEINS)[42]; 6) Automated Water Extraction Index Shadow (AWEIS)[42]; and 7) Linear Discriminant Analysis Water Index (LDAWI)[43]. The calculation formula of each water index is shown in Appendix Table A2.

## 2.3. Obtaining cloud-free label

As can be seen from Figure 1, although the SAR image is not interfered by clouds, the corresponding image only has coarse labels obtained by the unsupervised Otsu threshold method. Meanwhile, multispectral images have fine manual labels but have large areas covered by clouds, which are defined as invalid areas. Even for SAR images without cloud obstruction, these invalid regions cannot participate in training, it will exacerbate the problem of labeled sample scarcity and class imbalance in water segmentation. Therefore, we propose a Multi-Model Decision Fusion (MMDF) method to automatically obtain cloud-free labels based on the fine manual labels of multispectral images. The framework of MMDF is shown in Figure 2.

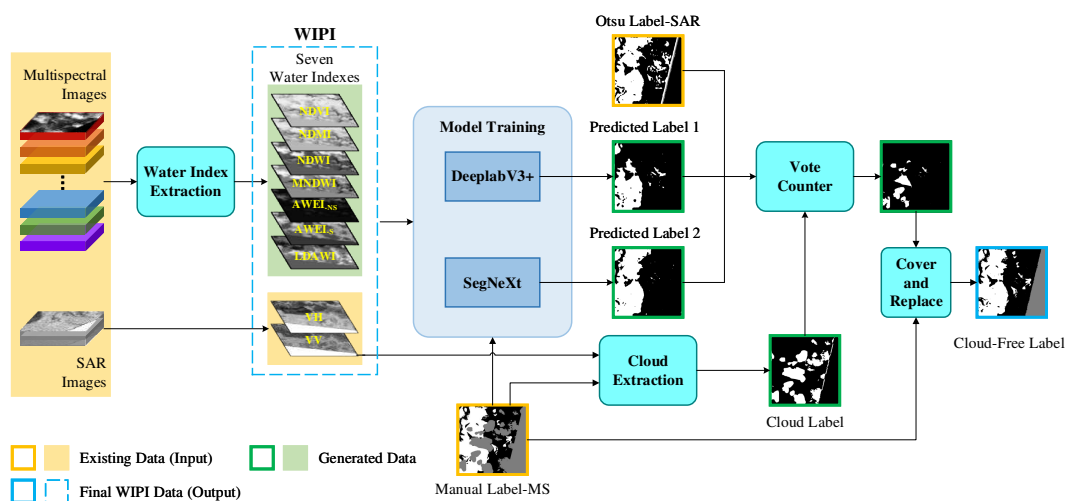


**Figure 2.** The framework of MMDF to automatically obtain cloud-free labels.

Since cloud and invalid region have the same label in the Manual label-MS, first, we use the VV band of the SAR image to extract the invalid region, and then remove the invalid region in the Manual

label-MS to get the Cloud Label with only the cloud part. On the other hand, seven extracted water indexes from multispectral images and VV and VH of SAR images are concatenated as the input to train the semantic segmentation models. In training, the Manual label-MS is used to calculate the loss function. Two state-of-the-art models of SegNeXt[24] and DeeplabV3+[19] are trained to get the Predicted Label 1 and Predicted Label 2, respectively. Next, based on the Cloud Label, we use Otsu Label-SAR, Predicted Label 1, and Predicted Label 2 for the cloud region to vote. Finally, we replace the label '-1' (cloud region) of Manual label-MS with the voting results label '0' (non-water) or '1' (water). In this way, the construction of the whole Water Index and Polarization Information (WIPI) dataset is completed. The WIPI dataset includes multi-modality images of nine-channel (seven water indexes + VV + VH) and the Cloud-Free Label automatically obtained by our proposed MMDF algorithm. The example instances of nine-channel and corresponding Ground Truth (Cloud-Free Label) are shown in Figure 3.

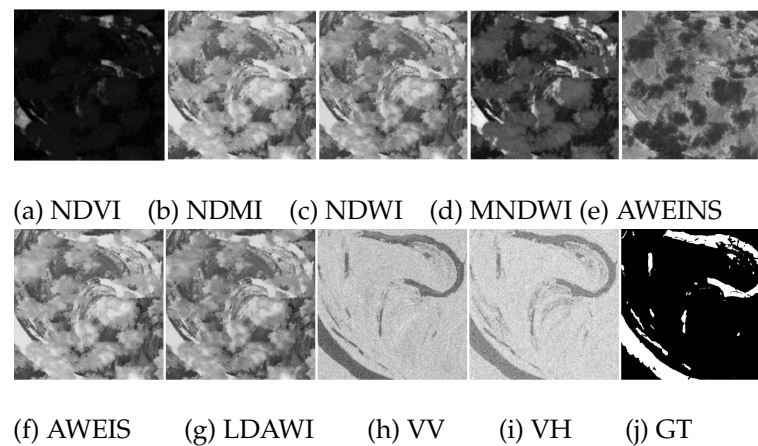


**Figure 3.** Example instances of nine-channel and Ground Truth (Cloud Free Label) of WIPI dataset.

### 3. Methodology

The framework of our proposed multi-Modality Fusion and Gated multi-Filter U-Net (MFGF-UNet) is shown in Figure 4. MFGF-UNet is an end-to-end u-shaped network, which mainly consists of four parts: 1) WIPI multi-modality data construction; 2) u-shaped encoder-decoder; 3) skip connection with channel attention; and 4) gated multi-filter inception module. The first part has been introduced in detail in Section 2, and the details of the remaining three parts are described in the following.

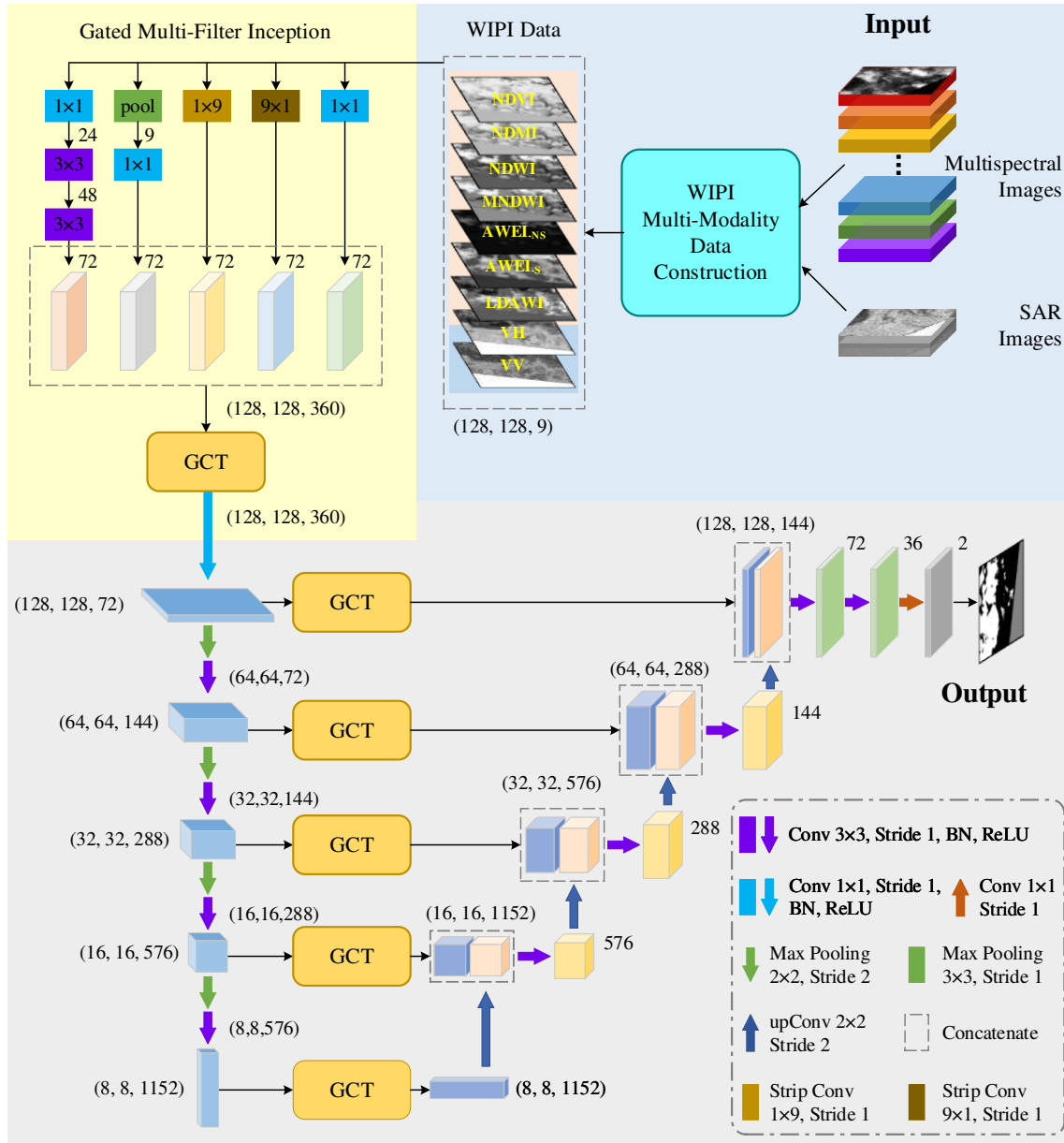


Figure 4. Illustration of the proposed MFGF-UNet framework.

### 3.1. U-shaped encoder-decoder

Due to relatively few labeled samples of water segmentation, we adopt a simple and efficient u-shaped encoder-decoder as the base architecture. In the encoder path, we design the four layers of max-pooling and ConvBR block, which repeatedly perform the following operations:

$$\tilde{x}^{(h/2, w/2, c)} = \text{maxPool}(x_l^{(h, w, c)}) \quad (1)$$

$$x_{l+1}^{(h/2, w/2, 2c)} = \text{ReLU}(\text{BN}(\text{Conv}_{3 \times 3}(\tilde{x}^{(h/2, w/2, c)}))) \quad (2)$$

where  $x_l^{(h, w, c)}$  indicates the feature map, the subscript  $l$  denotes the current layer, and the superscript  $(h, w, c)$  denotes the resolution and number of channels under the corresponding layer.  $\text{maxPool}(\cdot)$  denotes  $2 \times 2$  max-pooling with stride=2 for down-sampling the feature map of  $l$ -th layer.  $\text{Conv}_{3 \times 3}(\cdot)$  denotes  $3 \times 3$  convolution with stride=1 and the number of output channels is twice that of input



channels.  $\text{BN}(\cdot)$  and  $\text{ReLU}(\cdot)$  denote Batch Normalization[44] and Rectified Linear Units [45], respectively.

The decoder path also consists of four layers of up-convolution and ConvBR block, which can be expressed as:

$$\tilde{\mathbf{y}}^{(h,w,c/2)} = \text{upConv}(\mathbf{y}_{l+1}^{(h/2,w/2,c)}) \quad (3)$$

$$\mathbf{y}_l^{(h,w,c/2)} = \text{ReLU}(\text{BN}(\text{Conv}_{3 \times 3}(\text{Cont}(\hat{\mathbf{x}}_l^{(h,w,c/2)}, \tilde{\mathbf{y}}^{(h,w,c/2)})))) \quad (4)$$

where  $\text{upConv}(\cdot)$  denotes  $2 \times 2$  up-convolution with stride=2, it up-samples the input feature map to the double size while reducing the channel number by half. The ConvBR block of Eq. (4) is similar to Eq. (2), except that the output channel of  $\text{Conv}_{3 \times 3}(\cdot)$  is half the input channel number. The output of the up-convolution  $\tilde{\mathbf{y}}^{(h,w,c/2)}$  and the skip connections  $\hat{\mathbf{x}}_l^{(h,w,c/2)}$  are concatenated along the channel dimension by the  $\text{Cont}(\cdot)$  (concatenating operation) as the input of the ConvBR block. The last layer of the decoder is a  $1 \times 1$  convolution layer that maps the number of feature channels to the number of classes and produces the final segmentation map.

### 3.2. Skip connections with channel attention

As shown in Figure 4, we introduce the Gated Channel Transform (GCT)[46] module as the skip connections to fuse shallow features from the encoder with deep features from the decoder. Compared to traditional skip connections, adding the GCT module can adaptively adjust the weight of each channel and improve the performance of the whole network. GCT consists of three parts: Global Context Embedding, Channel Normalization, and Gating Adaptation, where Channel Normalization is a parameter-free operation. GCT places the learnable parameters in the Global Context Embedding and Gating Adaptation operations. The former collects global information via L2 norm and assigns a learnable weight control parameter for each channel. The latter introduces a competitive mechanism between channels via channel normalization and assigns a learnable gating parameter and bias for each channel. The last stage of GCT uses tanh to activate the attention vector and get enhanced features.

Let  $x_l^{(h,w,c)}$  be the input feature of GCT of the current layer  $l$ , and  $\alpha, \gamma$  and  $\beta$  be the trainable parameters. The calculation process of GCT is as follows:

$$\text{GCE} = \alpha \times L_2(\mathbf{x}_l^{(h,w,c)}) \quad (5)$$

$$\text{CN} = \frac{L_2(\text{GCE})}{\text{GCE} \times \sqrt{c}} \quad (6)$$

$$\hat{\mathbf{x}}_l^{(h,w,c)} = \tanh(\gamma \times \text{CN} + \beta) \times \mathbf{x}_l^{(h,w,c)} + \mathbf{x}_l^{(h,w,c)} \quad (7)$$

where  $L_2(\cdot)$  denotes L2 norm, GCE denotes Global Context Embedding, CN denotes Channel Normalization,  $c$  is the number of channel, and  $\hat{\mathbf{x}}_l^{(h,w,c)}$  denotes the output feature of GCT.

### 3.3. Gated multi-filter inception module

For the gated multi-filter inception module upwards of the U-shape backbone, We design five different forms of filters with different kernel sizes, including the  $1 \times 1$  convolution, the stacking of max pooling and  $1 \times 1$  convolution, the stacking of  $1 \times 1$  and two  $3 \times 3$  convolutions, and two strip convolutions respective of  $1 \times 9$  and  $9 \times 1$  kernel size. The receptive fields of the five filters cover multi-scales of small, medium and large, which aligns with the intuition that water bodies should be processed at various scales. The number of output channels of each filter is increased to five times that of input channels, and then the outputs of all filters are concatenated. Instead of directly using the concatenated feature as the output of Inception, we introduce a GCT module and  $1 \times 1$  dimensionality reduction convolution for adaptively aggregating features by attention and gated mechanism, so that the next stage can better abstract features from different scales simultaneously.

The detail of Inception module is depicted in the light-yellow background part of Figure 4, which performs the following operations:

$$\tilde{x}_{in}^{(128,128,360)} = \text{Cont}(F_1(x_{in}), F_2(x_{in}), F_3(x_{in}), F_4(x_{in}), F_5(x_{in})) \quad (8)$$

$$x_{l=1}^{(128,128,72)} = \text{ReLU}(\text{BN}(\text{Conv}_{1 \times 1}(\text{GCT}(\tilde{x}_{in}^{(128,128,360)})))) \quad (9)$$

where  $x_{in} \in R^{128 \times 128 \times 9}$  denotes WIPI data,  $F_{i=1,\dots,5}(\cdot)$  respectively denotes five designed filters,  $\text{GCT}(\cdot)$  denotes Gated Channel Transform, and its specific implementation is shown in Eq.(5)-(7).  $\text{Conv}_{1 \times 1}(\cdot)$  denotes  $1 \times 1$  convolution with stride=1 and the number of output channels is one fifth that of input channels.

## 4. Experiments

### 4.1. Dataset and Pre-processing

**WIPI multi-modality dataset.** In this work, we use three datasets to comprehensively verify the performance of the proposed MFGF-UNet method. Among them, our constructed Water Index and Polarization Information (WIPI) dataset is used as the main dataset, and ablation experiments and comparison experiments are performed on WIPI. The WIPI dataset consists of seven water indexes based on multispectral images and two polarization information from SAR images, and the Cloud-Free Label automatically obtained by our proposed algorithm. The construction details of WIPI are given in the aforementioned Section 2. We have released the WIPI dataset<sup>2</sup>.

**Chengdu dataset.** The Chengdu dataset<sup>3</sup>[47] is a remote sensing multispectral image captured by the Sentinel-2 satellite in April 2018 in Chengdu City of China and its surrounding areas (over 15,000  $km^2$ ). The dataset consists of images with five sensitive bands to water reflection and corresponding ground truth labels. The five bands are: bands 2-4 (R, G, and B), band 8 (near-infrared, NIR), and band 12 (short-wave infrared, SWIR).

**GF2020 dataset.** The GF2020 dataset [https://drive.google.com/file/d/1oHyzNfHe\\_F3MeeUQUoni9dh1LFI\\_N6RS/view?usp=sharing](https://drive.google.com/file/d/1oHyzNfHe_F3MeeUQUoni9dh1LFI_N6RS/view?usp=sharing)[48] is the high-resolution optical dataset from the GF-2 satellite for Track 5 (automatic water-body segmentation in optical satellite images) of the 2020 Gaofen Challenge. The dataset consists of images with RGB three channels and corresponding ground truth labels.

An example instance of the WIPI dataset is shown in the aforementioned Figure 3. Figure 5 and Figure 6 are example instances of datasets Chengdu and GF2020 respectively.

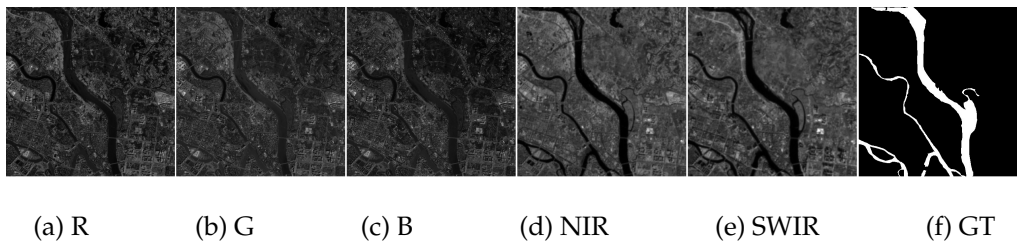


**Figure 5.** Example instances of five-channel and Ground Truth of Chengdu dataset.

<sup>2</sup> <https://github.com/Dataset-RFGroup/WIPI-Dataset>

<sup>3</sup> <https://github.com/SCouly/Sentinel-2-Water-Segmentation>

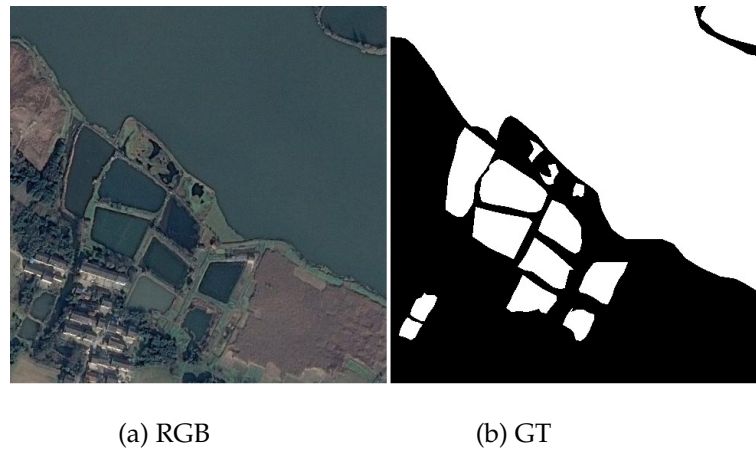


**Figure 6.** Example instances of optical RGB image and Ground Truth of GF2020 dataset.

The image size in each of the three datasets, as well as the number of train, validation, and test sample sets, are shown in Table 1.

**Table 1.** The basic information of the three datasets.

Dataset	Image size	Number of Dataset			
		Total	Train set	Val set	Test set
WIPI	(512,512,9)	446	221	85	140
Chengdu	(512,512,5)	1681	1008	336	337
GF2020	(492,492,3)	1000	600	200	200

"Image size" is in the form of (height, width, channel).

**Pre-processing.** The pre-processing steps for three datasets mainly include two key stages: 1) Normalization and standardization. We calculate the minimum and maximum values for each dataset and normalized the pixel values by min-max normalization to  $[0,1]$ . And then, we standardize the pixel values by subtracting the mean and then dividing by the standard deviation, to ensure a consistent value distribution across the entire dataset. 2) Sample Cropping. In this stage, we used a sliding approach to crop a single image into multiple patches of  $128 \times 128$ , with an overlap of 32 between adjacent patches. For the GF2020 dataset, since its height and width are  $492 \times 492$ , when cropping with a  $128 \times 128$  size, the patches at the rightmost and bottom edges will have an overlap greater than 32 pixels. During testing, after the predictions are complete, all patches from a single image will be reassembled to the original image size for evaluation.

#### 4.2. Experimental Setup and Evaluation Metrics

For MFGF-UNet, we set epoch as 200, and batch size as 32. The initial learning rate  $lr = 1e-4$ , and then  $lr$  is decayed to  $0.99 \times lr$  every 5 epochs. A cross-entropy loss function is employed. The model is trained with Adam optimizer with momentum 0.99 and weight decay  $5e-4$ . All experiments are conducted based on an Ubuntu system with Python 3.7, PyTorch 1.11.0, CUDA 11.3, and Nvidia RTX3090Ti GPU with memory of 24GB. The code and trained models are available at GitHub<sup>4</sup>.

Three widely used measures, accuracy (ACC), F1 score (F1), and Mean Intersection over Union (MIoU) are adopted as criteria to quantitatively evaluate the performance of the different methods, which are calculated as follows:

$$\text{Accuracy} = \frac{TP + TN}{TP + TN + FN + FP} \quad (10)$$

<sup>4</sup> <https://github.com/Code-RFGroup/MFGF-UNet>

$$\text{Recall} = \frac{TP}{TP + FN} \quad (11)$$

$$\text{Precision} = \frac{TP}{TP + FP} \quad (12)$$

$$F1 = \frac{2 \times \text{Recall} \times \text{Precision}}{\text{Recall} + \text{Precision}} \quad (13)$$

$$MIOU = \frac{1}{k+1} \sum_{i=0}^k \frac{TP}{TP + FP + FN} \quad (14)$$

where  $k$  indicates the number of classes. The confusion matrix between the predicted result and a given ground truth is calculated, consisting of true positives (TP), true negatives (TN), false positives (FP), and false negatives (FN). The positive and negative represent water and non-water, respectively. For ACC, MIOU and F1, a higher score means better performance. For all experiments, each algorithm runs three times independently, and the average results are given. Except for ACC, MIOU and F1 to evaluate the performance, we measure the complexity of different models using the number of parameters (Param) and one billion floating-point operations per second (GFLOPs).

#### 4.3. Ablation studies

In order to explore the influence of different factors on MFGF-UNet performance, we conduct ablation studies on WIPI dataset and discuss four factors below.

**AS1: Effect of u-shaped encoder-decoder (Enc&Dec).** In the model with Enc&Dec, we replaced GCT skip connection with a direct skip connection and removed the gated multi-filter inception module. Only the U-shaped encoder-decoder part is remained, and the input of the encoder is nine channels of WIPI data.

**AS2: Effect of GCT skip connection (GCT).** In the model with Enc&Dec and GCT, we only removed the gated multi-filter inception module.

**AS3: Effect of gated multi-filter inception (Inception).** In the model with Enc&Dec and Inception, we only replaced GCT skip connection with a direct skip connection.

Table 2 shows that above three factors influence both segmentation results and complexity. In AS1, which removes all two improved modules, the F1 score reaches 91.26% with a decrease of 0.65% compared to MFGF-UNet. This result shows that our improvements are effective. In AS2 and AS3, where the GCT or Inception module is individually removed, there is a decrease of 0.12% and 0.48% respectively. It indicates the proposed Inception module contributes more than the GCT module.

**Table 2.** Ablation studies of three factors on WIPI dataset.

Method	Enc & Dec	Inception	GCT	ACC(%)	MIOU(%)	F1(%)	Param(M)	GFLOPs
AS1	✓			98.09(±0.04)	83.92(±0.31)	91.26(±0.18)(↓0.65)	27.36	15.74
AS2	✓	✓		98.21(±0.01)	84.82(±0.15)	91.79(±0.08)(↓0.12)	27.53	21.04
AS3	✓		✓	98.13(±0.03)	84.21(±0.28)	91.43(±0.16)(↓0.48)	27.37	15.75
MFGF-UNet	✓	✓	✓	<b>98.22(±0.01)</b>	<b>85.03(±0.18)</b>	<b>91.91(±0.11)</b>	27.53	21.05

↓ : The degree of F1 decrease is from the comparison with MFGF-UNet.

**AS4: Effect of different modalities.** To analyze the impact of the different modalities on MFGF-UNet performance, we modified MFGF-UNet by using the different modality data as input, while keeping other parts the same. There are a total of four modalities: SAR, MSI, WI, and WIPI, where SAR denotes the polarization information of VV and VH from SAR, MSI denotes the spectrum of 13 bands from MSI, WI denotes the extracted seven water indexes from raw MSI, and WIPI denotes the water index and polarization information, including VV, VH and seven water indexes. For input images of all modalities, Cloud-Free Label is used as ground truth to eliminate the impact of different labels. From the results given in Table 3, it can be seen that the segmentation performance of the SAR is relatively poor, with ACC, MIOU, and F1 scores reaching only 95.22%, 63.18%, and 77.68%, respectively.

The segmentation results using MSI data are far better than SAR. However, given that MSI data has the largest band dimension, the model requires the highest amount of parameters and calculations, in which Param and GFLOPs reached 57.43 and 43.79, respectively. It is worth noting that the results using WI extracted from MSI data are better than those using original MSI data. The improvement of WI on average ACC, MIoU and F1 are 0.24%, 1.59% and 0.97% respectively. Additionally, using WI reduces the dimension of original data, which obtain a significant decrease in both Param and GFLOPs. Our WIPI data not only leverages the extracted water index, but also fuses the multi-modality of hyperspectral and SAR, thereby achieving superior results, with average ACC, MIoU, and F1 reaching 98.22%, 85.03%, and 91.91%, respectively.

Table 3. Ablation studies of different modalities on WIPI dataset.

Method	Modality	No. channel	ACC(%)	MIoU(%)	F1(%)	Param(M)	GFLOPs
MFGF-UNet	SAR	2	95.52(±0.06)	63.18(±0.60)	77.68(±0.79)(↓14.23)	1.36	1.04
	MSI	13	97.55(±0.04)	79.79(±0.29)	88.76(±0.18)(↓3.15)	57.43	43.79
	WI	7	97.79(±0.05)	81.38(±0.39)	89.73(±0.24)(↓2.18)	16.65	12.71
	WIPI	9	98.22(±0.01)	85.03(±0.18)	91.91(±0.11)	27.53	21.04

↓ : The degree of F1 decrease is from the comparison with WIPI.

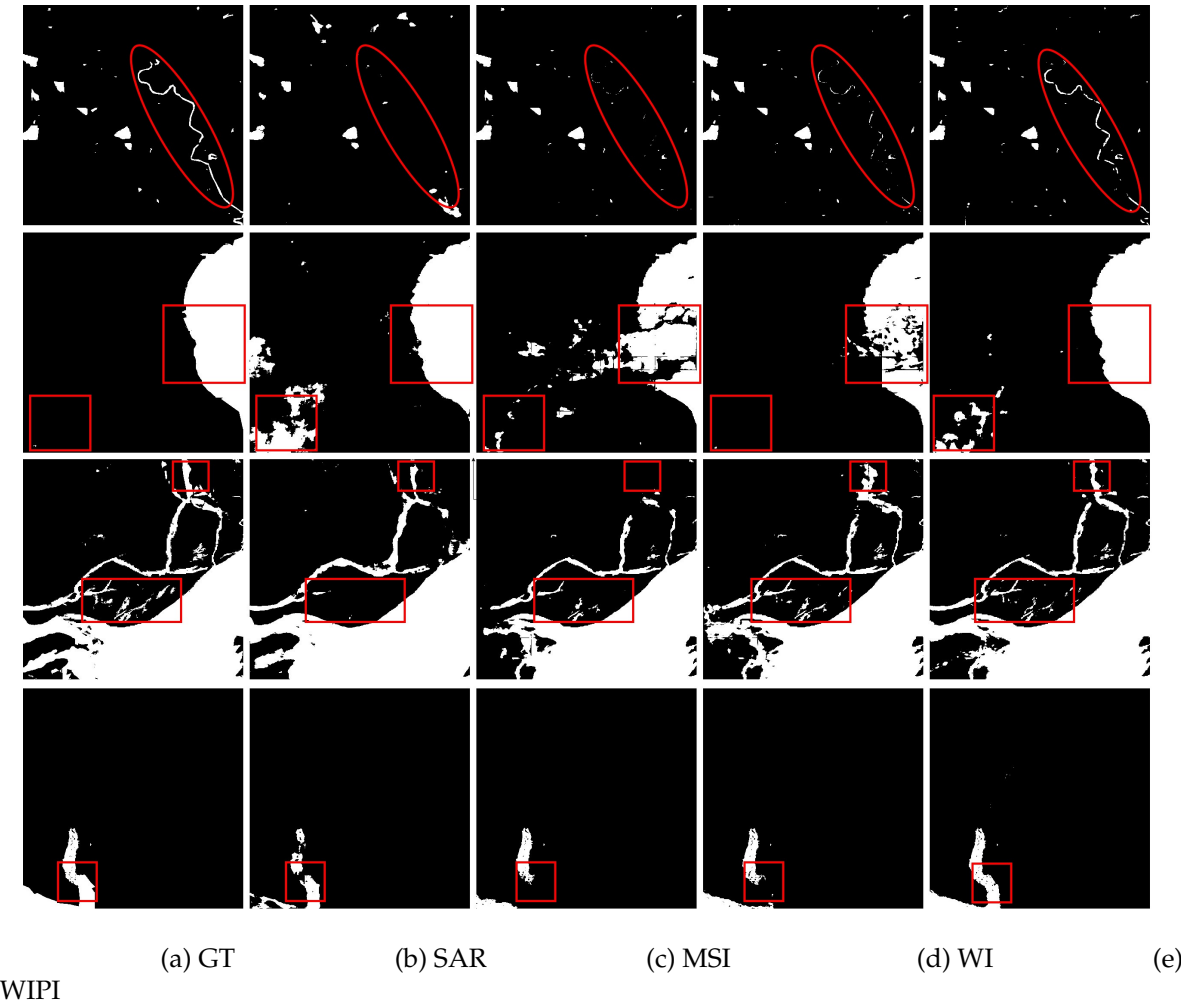


Figure 7. Visual comparisons between different modalities.

Moreover, visual comparisons between different modalities are shown in Figure 7 with the significant differences highlighted in the red line. It can be seen that if only single-modal SAR or MSI data are used, it is easy to lose the details of water bodies, such as slender rivers. At the same time,



using only WI data may lead to false detections with an extended range. Conversely, our WIPI can segment water bodies in a more consistent and complete manner.

#### 4.4. Comprehensive comparison with other methods

The proposed MFGF-UNet compare with six other state-of-the-art approaches, which are FCN-8s [12], U-Net[14], DeepLabV3+[19], BASNet[20], DUPNet[1], and SegNeXt[24]. For all other comparison methods, the parameters are set according to the corresponding original work. All methods take  $128 \times 128 \times C$  as the input size, where  $C$  is the number of channels corresponding to different dataset.

To verify the effectiveness of the constructed WIPI dataset and proposed MFGF-UNet model, we trained the above seven models on the two datasets Sen1Floods11 and WIPI, respectively. Sen1Floods11 dataset consists of images with 15 channels (VV, VH, and 13 multispectral bands) and the Manual Label-MS. WIPI dataset consists of images with 9 channels (VV, VH, and 7 water indexes) and the Cloud-Free Label. Except for ACC, MIoU, and F1 performance, we measure the complexity of different models using Param and GFLOPs. All results on two datasets are summarized in Table 4.

The experimental results in the table 4 show that when the Sen1Floods11 is replaced with our WIPI, the segmentation performance of all seven approaches has been significantly improved, among which the top three highest improvements are DUPNet, our MFGF-UNet, and U-Net, which average F1 scores increased by 11.30%, 9.23% and 7.09%, respectively. Meanwhile, given that the channel dimension is reduced from 15 to 7, the amount of parameters and calculations of all models have been reduced. Especially for our MFGF-UNet, using the WIPI dataset can reduce Param and GFLOPs by 48.93 and 37.32, respectively.

**Table 4.** Segmentation quantitative results and complexity of seven approaches on Sen1Floods11 and WIPI datasets.

Method	Dataset	No. channel	ACC(%)	MIoU(%)	F1(%)	Param(M)	GFLOPs
FCN-8s[12]	Sen1Floods11	15	96.04(±0.28)	68.12(±1.91)	81.02(±1.36)	46.25	2.01
	WIPI	9	96.83(±0.06)	73.95(±0.62)	85.02(±0.41)(↑4.00)	46.24	<b>1.98</b>
U-Net[14]	Sen1Floods11	15	96.53(±0.46)	72.84(±2.47)	84.26(±1.64)	49.89	26.91
	WIPI	9	98.09(±0.04)	84.07(±0.21)	91.35(±0.12)(↑7.09)	49.89	26.69
DeepLabv3+[19]	Sen1Floods11	15	96.43(±0.34)	71.88(±1.91)	83.62(±1.28)	6.43	2.10
	WIPI	9	97.37(±0.03)	78.22(±0.33)	87.78(±0.21)(↑4.16)	<b>6.43</b>	2.09
BASNet[20]	Sen1Floods11	15	97.30(±0.06)	78.14(±0.17)	87.73(±0.10)	87.08	31.99
	WIPI	9	97.91(±0.07)	82.92(±0.45)	90.66(±0.27)(↑2.93)	87.07	31.93
DUPNet[1]	Sen1Floods11	15	95.16(±0.24)	66.06(±1.18)	79.55(±0.86)	49.87	69.20
	WIPI	9	98.01(±0.07)	83.23(±0.66)	90.85(±0.40)(↑11.30)	49.86	69.17
SegNeXt[24]	Sen1Floods11	15	96.67(±0.10)	72.15(±1.08)	83.81(±0.73)	27.54	2.02
	WIPI	9	97.11(±0.17)	76.38(±1.21)	86.60(±0.78)(↑2.79)	27.54	2.01
MFGF-UNet(ours)	Sen1Floods11	15	96.11(±0.53)	70.52(±2.64)	82.68(±1.84)	76.46	58.37
	WIPI	9	<b>98.22(±0.01)</b>	<b>85.03(±0.18)</b>	<b>91.91(±0.11)(↑9.23)</b>	27.53	21.05

↑ : The degree of F1 increase is from the comparison with the corresponding method on Sen1Floods11.

To further compare the advantages of WIPI over Sen1Floods11, we visualize the ground truth of two datasets and the predicted results of U-Net, DUPNet, SegNeXt and our MFGF-UNet in Figure 8. Among the six comparison methods, DUPNet and U-Net achieve the second and third best results after our method, and SegNeXt is the latest method. It can be observed that utilizing the WIPI dataset helps to eliminate some of the interference in the Sen1Floods11 dataset, such as shadows and cloud cover, thereby obtaining better segmentation results, especially for blocky, stripe-like, and patchy water bodies.

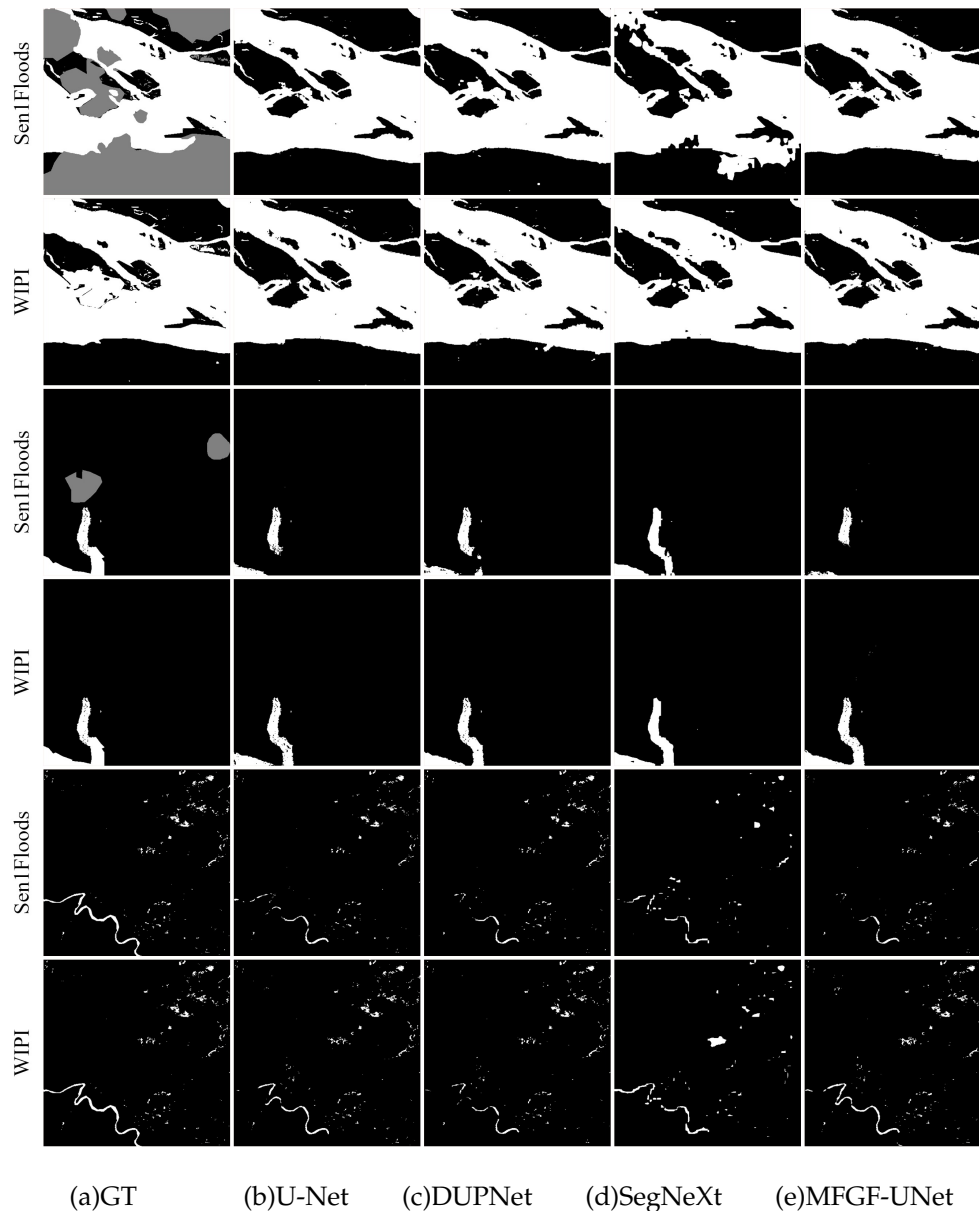


**Figure 8.** Visual comparisons of segmentation results from four approaches on Sen1Floods11 and WIPI datasets.

In addition to the improvement brought by the constructed WIPI dataset, the results in Table 4 also demonstrate that our method achieves the best performance against six state-of-the-art approaches with the ACC, MIoU, and F1 of 98.22%, 85.03%, and 91.91%, respectively. U-Net achieves an F1 score of 91.35% on WIPI dataset, second only to our MFGF-UNet, but Param and GFLOPs of U-Net are 22.36 and 5.64 more than our method respectively. Although Deeplabv3+ has the smallest model size, its segmentation performance on the WIPI dataset is much lower than MFGF-UNet, with a 4.13% drop in F1 score.

Figure 9 shows the segmentation results and corresponding zoom-in details on WIPI dataset from MFGF-UNet and six comparison methods. For the BASNet and DUPNet methods, many details such as slender rivers are missed, indicating that these models can only generate high-confidence predictions for large water areas. The segmentation results of SegNeXt are not precise enough because many small water bodies, particularly exhibiting jagged edges, are missed. Compared to other models, our method produces clearer and more accurate prediction maps for large water bodies, as well as slender rivers.

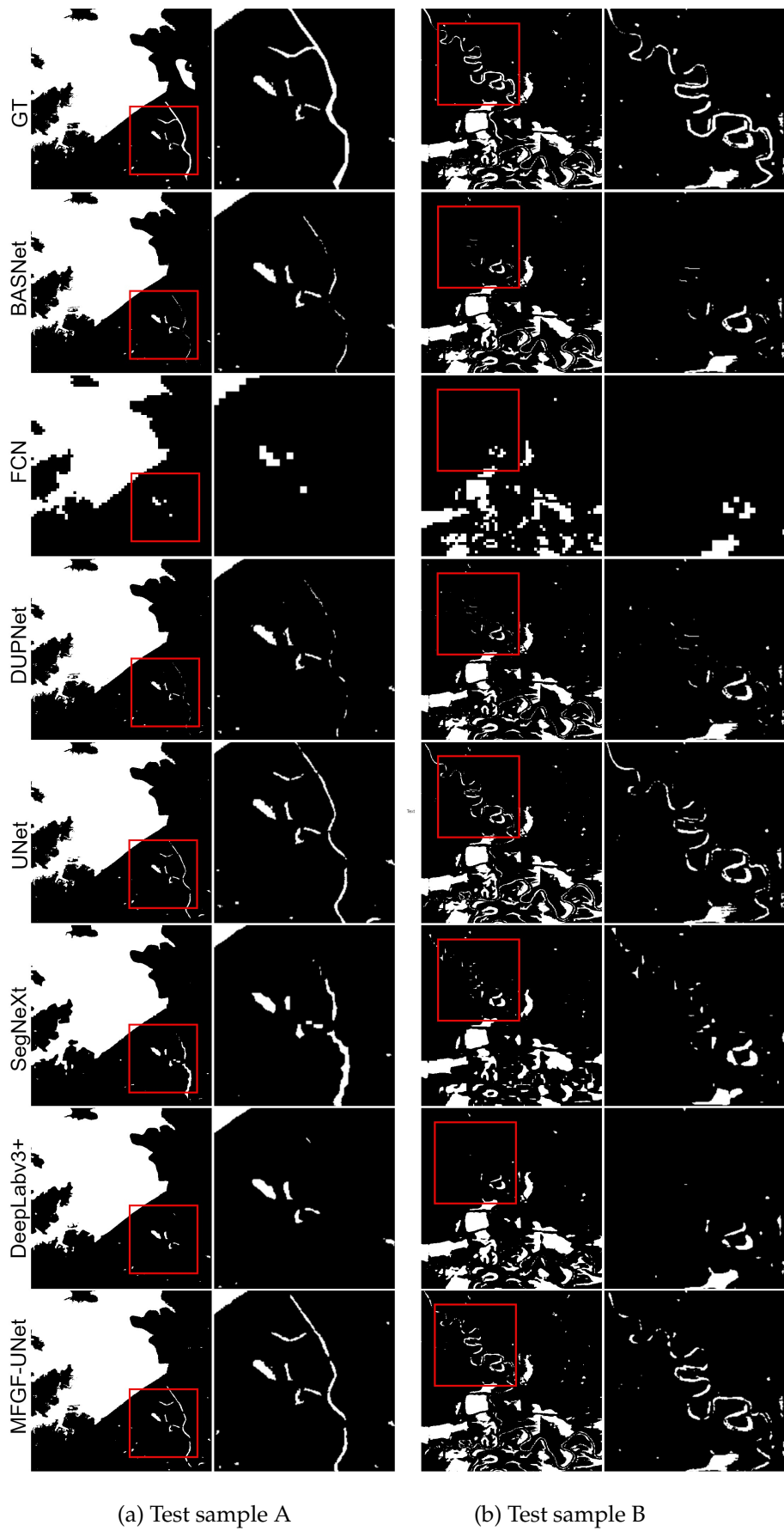


**Figure 9.** Visual comparisons of segmentation results and corresponding zoom-in details from seven approaches on WIPi dataset.

#### 4.5. Evaluation of the model robustness

Compared with the WIPI dataset, Chengdu and GF2020 datasets have different modalities, the former is a 5-channel multispectral image, and the latter is a high-resolution optical image. Moreover, these two datasets were captured from different sensors at different times while covering different ground ranges. Therefore, we conducted experiments of all methods on Chengdu and GF2020 to evaluate the robustness of the proposed MFGF-UNet model. The experimental results are shown in Table 5. It can be observed that on both the Chengdu and GF2020 datasets, MFGF-UNet outperforms FCN, UNet, Deeplabv3+, and SegNeXt models in performance. Although on the Chengdu dataset, MFGF-UNet has a 0.66% lower F1 score than BASNet, and on the GF2020 dataset, it has a 0.91% and 1.02% lower F1 score than BASNet and DUPNet, respectively, MFGF-UNet exhibits obvious lower complexity than BASNet and DUPNet. It is noteworthy that DUPNet only performs well on GF2020 dataset, and the results on Chengdu dataset are not very good.

**Table 5.** Segmentation quantitative results and complexity of seven approaches on Chengdu and GF2020 datasets.

Method	DataSet	ACC	MIoU	F1	Params (M)	GFLOPs
FCN-8s[12]	Chengdu	98.56( $\pm 0.01$ )	45.78( $\pm 0.76$ )	62.71( $\pm 0.64$ )	46.25	1.96
	GF2020	93.12( $\pm 0.01$ )	70.83( $\pm 0.22$ )	82.93( $\pm 0.15$ )	46.25	1.95
U-Net[14]	Chengdu	98.91( $\pm 0.01$ )	58.02( $\pm 0.61$ )	73.42( $\pm 0.49$ )	49.88	26.54
	GF2020	93.69( $\pm 0.11$ )	72.72( $\pm 0.77$ )	84.10( $\pm 0.51$ )	49.88	26.46
DeepLabv3+[19]	Chengdu	98.86( $\pm 0.01$ )	55.96( $\pm 0.50$ )	71.76( $\pm 0.41$ )	6.43	2.09
	GF2020	92.56( $\pm 0.16$ )	68.86( $\pm 0.90$ )	81.55( $\pm 0.63$ )	6.43	2.09
BASNet[20]	Chengdu	98.90( $\pm 0.01$ )	<b>59.69</b> ( $\pm 0.12$ )	<b>74.75</b> ( $\pm 0.09$ )	87.07	31.89
	GF2020	93.45( $\pm 0.16$ )	74.11( $\pm 0.35$ )	85.13( $\pm 0.23$ )	87.07	31.87
DUPNet[1]	Chengdu	98.87( $\pm 0.01$ )	56.87( $\pm 0.72$ )	72.50( $\pm 0.58$ )	49.86	69.16
	GF2020	<b>93.79</b> ( $\pm 0.06$ )	<b>74.27</b> ( $\pm 0.09$ )	<b>85.23</b> ( $\pm 0.06$ )	49.86	69.15
SegNeXt[24]	Chengdu	98.84( $\pm 0.01$ )	55.29( $\pm 0.13$ )	71.21( $\pm 0.11$ )	27.54	2.01
	GF2020	93.06( $\pm 0.09$ )	72.03( $\pm 0.26$ )	83.74( $\pm 0.17$ )	27.54	2.01
MFGF-UNet	Chengdu	<b>98.91</b> ( $\pm 0.01$ )	58.85( $\pm 0.10$ )	74.09( $\pm 0.08$ )	8.50	6.49
	GF2020	93.63( $\pm 0.09$ )	72.73( $\pm 0.45$ )	84.21( $\pm 0.30$ )	3.06	2.36

Figure 10 and 11 show the segmentation results and corresponding zoom-in details on Chengdu and GF2020 datasets from MFGF-UNet and six comparison methods. The Chengdu dataset comprises a greater number of slender water areas, while the GF2020 dataset includes more extensive and continuous water areas. For the DUPNet method, it achieved the highest F1 score on the GF2020 dataset but exhibited relatively lower performance on the Chengdu dataset. This result can be reasonably explained by the figures that DUPNet is not very good at detecting small water bodies, but has better performance on large water areas. Visualized results further illustrate our proposed MFGF-UNet excels in the segmentation of small water bodies and simultaneously proves effective in segmenting large water areas.

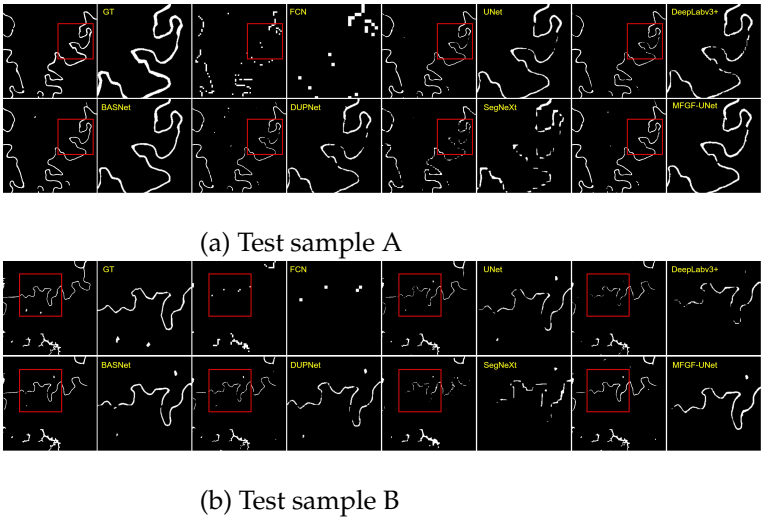


**Figure 10.** Visual comparisons of segmentation results and corresponding zoom in detail from seven approaches on Chengdu dataset.

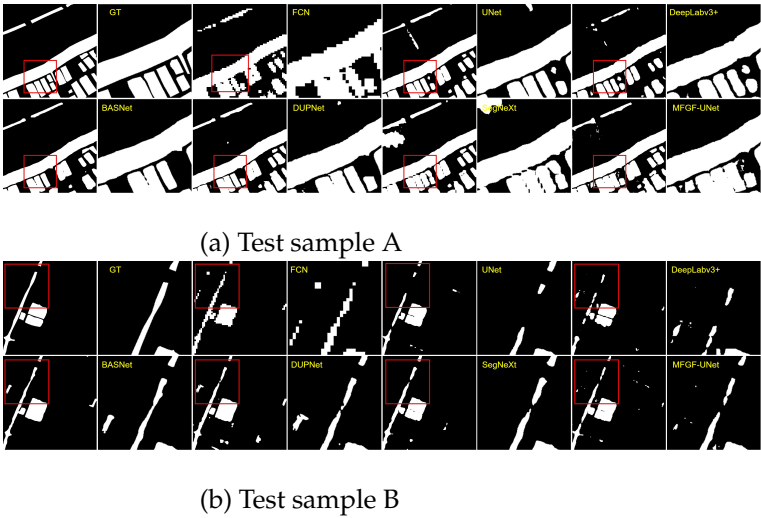


**Figure 11.** Visual comparisons of segmentation results and corresponding zoom in detail from seven approaches on GF2020 dataset.

The comprehensive comparison of the segmentation performance and complexity of the seven models on the three datasets is shown in Figure 12, where the x-axis represents GFLOPs, the y-axis represents F1, and the radius of the circle represents the parameter size of each model. The closer to the upper left corner and the smaller the radius indicate the better effectiveness and efficiency of the algorithm. The above results and analysis illustrate that our MFGF-UNet has achieved favorable performance with lower complexity and better robustness on three datasets.



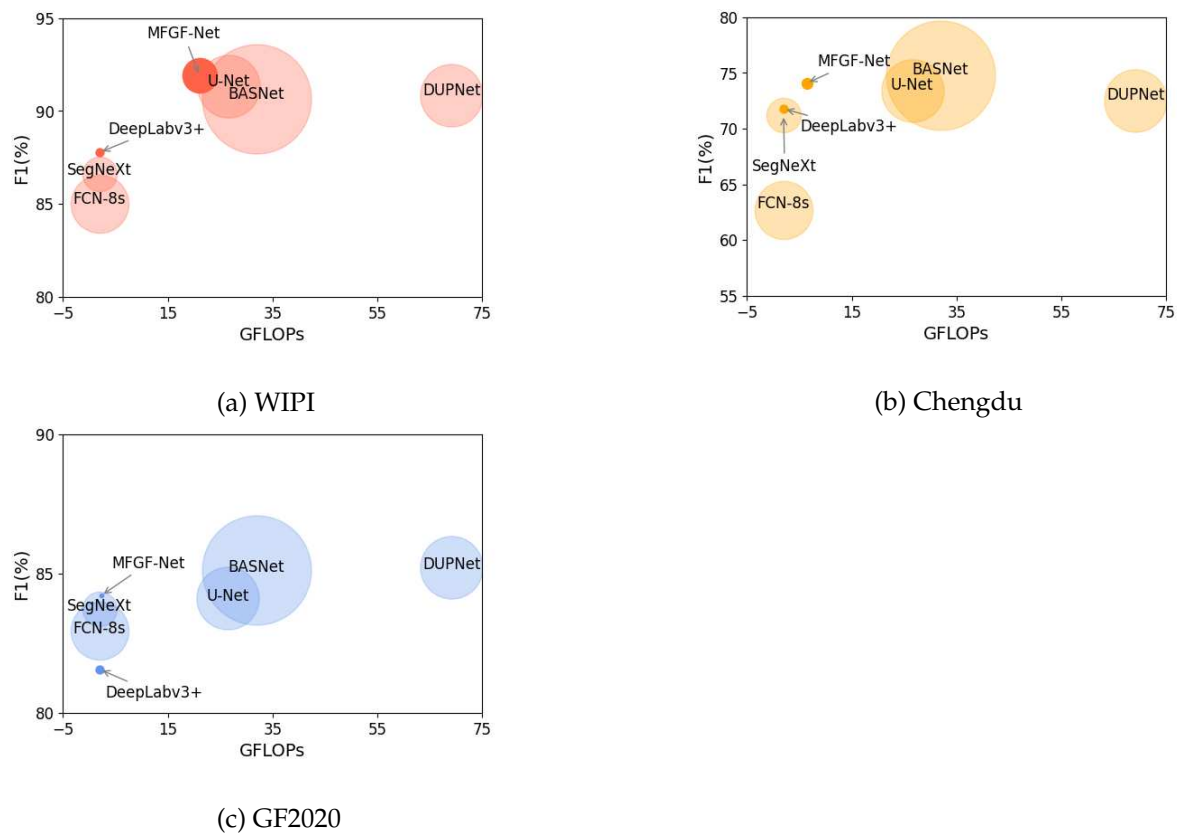


**Figure 12.** Param and GFLOPs vs. F1 of seven approaches on WIPI, Chengdu, and GF2020 datasets.

## 5. Discussion

As shown in the experiments in this work, the use of different modalities or used in different ways will have a great impact on water segmentation. For example, in Table 3, the same ground region and the same model, the F1 from lowest to highest is SAR, MSI, WI, and WIPI, which are 77.68%, 88.76%, 89.73% and 91.91%, respectively. Since the polarization information of SAR images cannot distinguish water, water-like surfaces and noise-like spots well, which F1 is the lowest. MSI provides 13 bands information with high resolution and less noise, so its F1 is 11.08% higher than that of SAR. As expected, multi-modality WIPI achieves the best results. For all seven methods, the average F1 on WIPI is 89.17% in Table 4. In Table 5, the average F1 on Chengdu (multispectral image with five bands) and GF2020 (high-resolution optical images) is 71.49% and 83.84%, respectively. Even if the differences in region and number of datasets are put aside, it also can be found that our constructed WIPI dataset performs best. It is worth noting that F1 of MSI is 0.97% lower than that of WI in Table 3. At the same time, in Table 4, the average F1 on Sen1Floods11 is 83.24%, which is 5.93% lower than that of WIPI. Even if the raw data for MSI and WI are both multispectral image with 13 bands, and the raw data for Sen1Floods11 and WIPI are the same multispectral and SAR image, how different modalities are analytically utilized will change the performance of model. The above results also verify the effectiveness of the water index we extracted.

Another reason for the lower performance on Sen1Floods11 is that the Manual Label-MS contains a large number of invalid areas, resulting in multi-modality results are lower than those of single-modality but using Cloud-Free Label, such as for the MFGF-UNet model, the F1 of single-modality MSI and WI is 88.76% and 89.73%, however, F1 of multi-modality Sen1Floods11 is only 82.68%.

The utilization of the water index could not only enhance the water information but also reduce the data dimension, thus decreasing the overall complexity of the model. For example, on WIPI (9 channels), Chengdu (5 channels), and GF2020 (3 channels) datasets, the proposed MFGF-UNet model

achieves F1 of 91.91%, 74.10%, 84.21% with GFLOPs 21.05, 6.49, and 2.36, respectively. As the input data dimensions are reduced, our model complexity is significantly reduced. This trend emanates from the meticulous design of our encoder, where the output feature channel count of the first network layer is eight times that of the input feature channels, and the subsequent network layers have an output channel count twice that of the input channels. It is evident that our model can dynamically adjust with a high degree of adaptability to accommodate varying scales of input data. Compared with the U-Net, which has better performance, F1 reaches 91.35%, 73.42%, and 84.10% with GFLOPs 26.69, 26.54, and 26.46, respectively. As the input data dimensions are reduced, the complexity of U-Net model is also decreasing (note that the unit of measurement is one billion). When the GFLOPs are only 24% and 9% of U-Net, our MFGF-UNet still achieves slightly better segmentation performance on Chengdu and GF2020 datasets. These results illustrate that besides the design of architecture, focusing on the data-level can also reduce the computational cost of the model.

## 6. Conclusions

In this work, we proposed an effective and efficient MFGF-UNet model for water area segmentation of remote sensing. We first analyzed the task's current challenges, and then designed corresponding strategies to address these issues. Concretely, we constructed a WIPI multi-modality dataset to overcome the shortcomings of single-modal data and enhance water information while reducing the channel dimension of data, the Cloud-Free Label provided in the dataset can also effectively alleviate the problem of labeled sample scarcity. For the issue that a single form or uniform kernel size cannot handle the variety in size and shape of water bodies, we proposed the gated multi-filter inception (GMF-Inception) module. Moreover, we utilized the attention mechanism by introducing the GCT skip connection and integrating GCT into GMF-Inception to further improve model performance. Extensive experiments on various three benchmarks, including WIPI (water index and SAR images), Chengdu (multispectral images) and GF2020 (optical images) datasets demonstrated that our MFGF-UNet model achieves favorable performance with lower complexity and better robustness against six competing approaches.

Moreover, since we focus on the data-level fusion in this work, yet data fusion includes different aspects such as data, features and decisions, we will continue to explore more effective and efficient methods from feature-level or decision-level to fuse multi-modality information for water area segmentation in future research. Meanwhile, we hope the release of a new dataset could help the researchers to develop and verify effective frameworks for water area segmentation and facilitate more breakthroughs in this field.

**Funding:** This work was supported by the National Natural Science Foundation of China (No. 62176196 and 62077038), the Key Research and Development Program of Shaanxi (No. 2023-YBNY-218 and 2023-YBNY-284), the Open Project Program of the State Key Laboratory of Multimodal Artificial Intelligence Systems (No. 202200021).

**Conflicts of Interest:** The authors declare no conflict of interest.

## Appendix A

### *Appendix A.1 The description of Sen1Floods11 dataset*

The Sen1Floods11 dataset consists of the raw Sentinel-1 SAR image (Sen1-SAR) and the raw Sentinel-2 multispectral image (Sen2-MS), where Sen1-SAR includes VV and VH two bands, and Sen2-MS includes 13 bands (1-8, 8A, 9-12) across all spectrums. The value, format and band description of Sen1Floods11 is shown in Appendix Table A1.

Table A1. Sen1Floods11 dataset description.

Modality	Value	Format	Bands	
SAR	Unit: dB	GeoTIFF 512 × 512 2 bands Float32	0: VV 1: VH	
MSI	Unit: TOA reflectance (scaled by 10000)	GeoTIFF 512 × 512 13 bands UInt16	0: B1 (Coastal) 1: B2 (Blue) 2: B3 (Green) 3: B4 (Red) 4: B5 (RedEdge-1) 5: B6 (RedEdge-2)	7: B8 (NIR) 8: B8A (Narrow NIR) 9: B9 (Water Vapor) 10: B10 (Cirrus) 11: B11 (SWIR-1) 12: B12 (SWIR-2) 6: B7 (RedEdge-3)

A.2 The description of used seven water indexes

In this work, we analyze the characteristics of the water index and extract seven different water indexes from 13 bands of raw MSI for constructing our WIPI dataset. The formula and description of the extracted seven water indexes are shown in Table A2.

Table A2. The formula and description of seven water indexes.

Index	Name	Formula	Description
1	Normalized Difference Vegetation Index (NDVI)[40]	$(B8-B4)/(B8+B4)$	High values indicate dense tree canopies, while low or negative values indicate urban areas and water bodies.
2	Normalized Difference Moisture Index (NDMI)[41]	$(B8A-B11)/(B8A+B11)$	Vegetation with higher values is relatively moist.
3	Normalized Difference Water Index (NDWI)[26]	$(B3-B8)/(B3+B8)$	Highlights water bodies, suppresses vegetation information; susceptible to the influence of object shadows.
4	Modified Normalized Difference Water Index (MNDWI)[27]	$(B3-B11)/(B3+B11)$	Eliminate the influence of buildings and land, high-light water bodies, and easily affected by shadows of objects.
5	Automated Water Extraction Index (Non-Shadow, AWEINS)[42]	$(4B3-4B11)/(0.25B8+2.75B12)$	Remove black buildings that are easily misclassified as water bodies.
6	Automated Water Extraction Index (Shadow, AWEIS)[42]	$B2+2.5B3-1.5(B8+B11)-0.25B12$	Suitable for scenes with a high amount of shadow.
7	Linear Discriminant Analysis Water Index (LDAWI)[43]	$1.7204+171B3+3B4-70B8-45B11-71B12$	Suitable for scenes where there is a large difference in spectral distribution between non-water and water bodies.

References

1. Liu, Z.; Chen, X.; Zhou, S.; Yu, H.; Guo, J.; Liu, Y. DUPnet: Water Body Segmentation with Dense Block and Multi-Scale Spatial Pyramid Pooling for Remote Sensing Images. *Remote Sensing* **2022**, *14*, 5567.
2. Konapala, G.; Kumar, S.V.; Ahmad, S.K. Exploring Sentinel-1 and Sentinel-2 diversity for flood inundation mapping using deep learning. *ISPRS Journal of Photogrammetry and Remote Sensing* **2021**, *180*, 163–173.
3. Li, Y.; Dang, B.; Zhang, Y.; Du, Z. Water body classification from high-resolution optical remote sensing imagery: Achievements and perspectives. *ISPRS Journal of Photogrammetry and Remote Sensing* **2022**, *187*, 306–327.
4. Liu, J.; Wang, Y. Water Body Extraction in Remote Sensing Imagery Using Domain Adaptation-Based Network Embedding Selective Self-Attention and Multi-Scale Feature Fusion. *Remote Sensing* **2022**, *14*, 3538.
5. Shen, X.; Wang, D.; Mao, K.; Anagnostou, E.; Hong, Y. Inundation extent mapping by synthetic aperture radar: A review. *Remote Sensing* **2019**, *11*, 879.
6. Longfei, S.; Zhengxuan, L.; Fei, G.; Min, Y. A review of remote sensing image water extraction. *Remote Sensing for Natural Resources* **2021**, *33*, 9–11.
7. Cao, M.; Mao, K.; Shen, X.; Xu, T.; Yan, Y.; Yuan, Z. Monitoring the spatial and temporal variations in the water surface and floating algal bloom areas in Dongting Lake using a long-term MODIS image time series. *Remote Sensing* **2020**, *12*, 3622.
8. Shetty, S.; Gupta, P.K.; Belgiu, M.; Srivastav, S. Assessing the effect of training sampling design on the performance of machine learning classifiers for land cover mapping using multi-temporal remote sensing data and google earth engine. *Remote sensing* **2021**, *13*, 1433.

9. Razaque, A.; Ben Haj Frej, M.; Almi'ani, M.; Alotaibi, M.; Alotaibi, B. Improved support vector machine enabled radial basis function and linear variants for remote sensing image classification. *Sensors* **2021**, *21*, 4431.
10. Li, A.; Fan, M.; Qin, G.; Xu, Y.; Wang, H. Comparative analysis of machine learning algorithms in automatic identification and extraction of water boundaries. *Applied Sciences* **2021**, *11*, 10062.
11. Acharya, T.D.; Subedi, A.; Lee, D.H. Evaluation of machine learning algorithms for surface water extraction in a Landsat 8 scene of Nepal. *Sensors* **2019**, *19*, 2769.
12. Long, J.; Shelhamer, E.; Darrell, T. Fully convolutional networks for semantic segmentation. In Proceedings of the Proceedings of the IEEE conference on computer vision and pattern recognition, 2015, pp. 3431–3440.
13. Simonyan, K.; Zisserman, A. Very deep convolutional networks for large-scale image recognition. *arXiv preprint arXiv:1409.1556* **2014**.
14. Ronneberger, O.; Fischer, P.; Brox, T. U-net: Convolutional networks for biomedical image segmentation. In Proceedings of the Medical Image Computing and Computer-Assisted Intervention–MICCAI 2015: 18th International Conference, Munich, Germany, October 5–9, 2015, Proceedings, Part III 18. Springer, 2015, pp. 234–241.
15. Cui, M.; Li, K.; Chen, J.; Yu, W. CM-Unet: A novel remote sensing image segmentation method based on improved U-Net. *IEEE Access* **2023**.
16. Wang, L.; Li, R.; Zhang, C.; Fang, S.; Duan, C.; Meng, X.; Atkinson, P.M. UNetFormer: A UNet-like transformer for efficient semantic segmentation of remote sensing urban scene imagery. *ISPRS Journal of Photogrammetry and Remote Sensing* **2022**, *190*, 196–214.
17. Chen, L.C.; Papandreou, G.; Kokkinos, I.; Murphy, K.; Yuille, A.L. Semantic image segmentation with deep convolutional nets and fully connected crfs. *arXiv preprint arXiv:1412.7062* **2014**.
18. Chen, L.C.; Papandreou, G.; Kokkinos, I.; Murphy, K.; Yuille, A.L. Deeplab: Semantic image segmentation with deep convolutional nets, atrous convolution, and fully connected crfs. *IEEE transactions on pattern analysis and machine intelligence* **2017**, *40*, 834–848.
19. Chen, L.C.; Zhu, Y.; Papandreou, G.; Schroff, F.; Adam, H. Encoder-decoder with atrous separable convolution for semantic image segmentation. In Proceedings of the Proceedings of the European conference on computer vision (ECCV), 2018, pp. 801–818.
20. Qin, X.; Zhang, Z.; Huang, C.; Gao, C.; Dehghan, M.; Jagersand, M. Basnet: Boundary-aware salient object detection. In Proceedings of the Proceedings of the IEEE/CVF conference on computer vision and pattern recognition, 2019, pp. 7479–7489.
21. He, K.; Zhang, X.; Ren, S.; Sun, J. Deep residual learning for image recognition. In Proceedings of the Proceedings of the IEEE conference on computer vision and pattern recognition, 2016, pp. 770–778.
22. Huang, G.; Liu, Z.; Van Der Maaten, L.; Weinberger, K.Q. Densely connected convolutional networks. In Proceedings of the Proceedings of the IEEE conference on computer vision and pattern recognition, 2017, pp. 4700–4708.
23. Dosovitskiy, A.; Beyer, L.; Kolesnikov, A.; Weissenborn, D.; Zhai, X.; Unterthiner, T.; Dehghani, M.; Minderer, M.; Heigold, G.; Gelly, S.; et al. An image is worth 16x16 words: Transformers for image recognition at scale. *arXiv preprint arXiv:2010.11929* **2020**.
24. Guo, M.H.; Lu, C.Z.; Hou, Q.; Liu, Z.; Cheng, M.M.; Hu, S.M. Segnext: Rethinking convolutional attention design for semantic segmentation. *arXiv preprint arXiv:2209.08575* **2022**.
25. Akiva, P.; Purri, M.; Dana, K.; Tellman, B.; Anderson, T. H2O-Net: Self-supervised flood segmentation via adversarial domain adaptation and label refinement. In Proceedings of the Proceedings of the IEEE/CVF Winter Conference on Applications of Computer Vision, 2021, pp. 111–122.
26. McFeeters, S.K. The use of the Normalized Difference Water Index (NDWI) in the delineation of open water features. *International journal of remote sensing* **1996**, *17*, 1425–1432.
27. Xu, H. Modification of normalised difference water index (NDWI) to enhance open water features in remotely sensed imagery. *International journal of remote sensing* **2006**, *27*, 3025–3033.
28. Hu, J.; Shen, L.; Sun, G. Squeeze-and-excitation networks. In Proceedings of the Proceedings of the IEEE conference on computer vision and pattern recognition, 2018, pp. 7132–7141.
29. Woo, S.; Park, J.; Lee, J.Y.; Kweon, I.S. Cbam: Convolutional block attention module. In Proceedings of the Proceedings of the European conference on computer vision (ECCV), 2018, pp. 3–19.

30. Dai, J.; Qi, H.; Xiong, Y.; Li, Y.; Zhang, G.; Hu, H.; Wei, Y. Deformable convolutional networks. In Proceedings of the Proceedings of the IEEE international conference on computer vision, 2017, pp. 764–773.
31. Carion, N.; Massa, F.; Synnaeve, G.; Usunier, N.; Kirillov, A.; Zagoruyko, S. End-to-end object detection with transformers. In Proceedings of the Computer Vision–ECCV 2020: 16th European Conference, Glasgow, UK, August 23–28, 2020, Proceedings, Part I 16. Springer, 2020, pp. 213–229.
32. Yuan, Y.; Huang, L.; Guo, J.; Zhang, C.; Chen, X.; Wang, J. Ocnet: Object context network for scene parsing. *arXiv preprint arXiv:1809.00916* **2018**.
33. Fu, J.; Liu, J.; Tian, H.; Li, Y.; Bao, Y.; Fang, Z.; Lu, H. Dual attention network for scene segmentation. In Proceedings of the Proceedings of the IEEE/CVF conference on computer vision and pattern recognition, 2019, pp. 3146–3154.
34. Oktay, O.; Schlemper, J.; Folgoc, L.L.; Lee, M.; Heinrich, M.; Misawa, K.; Mori, K.; McDonagh, S.; Hammerla, N.Y.; Kainz, B.; et al. Attention u-net: Learning where to look for the pancreas. *arXiv preprint arXiv:1804.03999* **2018**.
35. Guan, Q.; Huang, Y.; Zhong, Z.; Zheng, Z.; Zheng, L.; Yang, Y. Diagnose like a radiologist: Attention guided convolutional neural network for thorax disease classification. *arXiv preprint arXiv:1801.09927* **2018**.
36. Xie, S.; Liu, S.; Chen, Z.; Tu, Z. Attentional shapecontextnet for point cloud recognition. In Proceedings of the Proceedings of the IEEE conference on computer vision and pattern recognition, 2018, pp. 4606–4615.
37. Su, W.; Zhu, X.; Cao, Y.; Li, B.; Lu, L.; Wei, F.; Dai, J. Vi-bert: Pre-training of generic visual-linguistic representations. *arXiv preprint arXiv:1908.08530* **2019**.
38. Xu, T.; Zhang, P.; Huang, Q.; Zhang, H.; Gan, Z.; Huang, X.; He, X. Attngan: Fine-grained text to image generation with attentional generative adversarial networks. In Proceedings of the Proceedings of the IEEE conference on computer vision and pattern recognition, 2018, pp. 1316–1324.
39. Bonafilia, D.; Tellman, B.; Anderson, T.; Issenberg, E. Sen1Floods11: A georeferenced dataset to train and test deep learning flood algorithms for sentinel-1. In Proceedings of the Proceedings of the IEEE/CVF Conference on Computer Vision and Pattern Recognition Workshops, 2020, pp. 210–211.
40. Rouse, J.W.; Haas, R.H.; Schell, J.A.; Deering, D.W.; et al. Monitoring vegetation systems in the Great Plains with ERTS. *NASA Spec. Publ* **1974**, 351, 309.
41. Jackson, R.D. Remote sensing of biotic and abiotic plant stress. *Annual review of Phytopathology* **1986**, 24, 265–287.
42. Feyisa, G.L.; Meilby, H.; Fensholt, R.; Proud, S.R. Automated Water Extraction Index: A new technique for surface water mapping using Landsat imagery. *Remote Sensing of Environment* **2014**, 140, 23–35.
43. Fisher, A.; Flood, N.; Danaher, T. Comparing Landsat water index methods for automated water classification in eastern Australia. *Remote Sensing of Environment* **2016**, 175, 167–182.
44. Ioffe, S.; Szegedy, C. Batch normalization: Accelerating deep network training by reducing internal covariate shift. In Proceedings of the International conference on machine learning. pmlr, 2015, pp. 448–456.
45. Glorot, X.; Bordes, A.; Bengio, Y. Deep sparse rectifier neural networks. In Proceedings of the Proceedings of the fourteenth international conference on artificial intelligence and statistics. JMLR Workshop and Conference Proceedings, 2011, pp. 315–323.
46. Yang, Z.; Zhu, L.; Wu, Y.; Yang, Y. Gated channel transformation for visual recognition. In Proceedings of the Proceedings of the IEEE/CVF conference on computer vision and pattern recognition, 2020, pp. 11794–11803.
47. Yuan, K.; Zhuang, X.; Schaefer, G.; Feng, J.; Guan, L.; Fang, H. Deep-learning-based multispectral satellite image segmentation for water body detection. *IEEE Journal of Selected Topics in Applied Earth Observations and Remote Sensing* **2021**, 14, 7422–7434.
48. Sun, X.; Wang, P.; Yan, Z.; Diao, W.; Lu, X.; Yang, Z.; Zhang, Y.; Xiang, D.; Yan, C.; Guo, J.; et al. Automated high-resolution earth observation image interpretation: Outcome of the 2020 Gaofen challenge. *IEEE Journal of Selected Topics in Applied Earth Observations and Remote Sensing* **2021**, 14, 8922–8940.

**Disclaimer/Publisher’s Note:** The statements, opinions and data contained in all publications are solely those of the individual author(s) and contributor(s) and not of MDPI and/or the editor(s). MDPI and/or the editor(s) disclaim responsibility for any injury to people or property resulting from any ideas, methods, instructions or products referred to in the content.